

The Growth and Crystalline Structure of Ultrathin Mn Films on Ni(111)

Jiaming Song and Wolfgang Kuch*

The growth and crystalline structure of ultrathin Mn films are studied in terms of thickness and temperature by scanning tunneling microscopy (STM) as well as medium- and low-energy electron diffraction. We show that the Mn films deposited at room temperature exhibit a thickness-dependent growth behavior with a layer-by-layer growth mode up to 5.3 monolayers. Two transitions in the growth mode can be observed in this range. Atomically resolved STM images of a submonolayer of Mn on Ni(111) reveal a lateral lattice distortion which becomes less significant after the islands form a wetting layer at room temperature. The low-temperature-deposited wetting layer shows a metastable lattice distortion which vanishes after annealing to room or higher temperatures. This phenomenon may be attributed to a temperature-dependent metastable arrangement of the Mn adlayer as well as the distinct interaction strength between Mn–Mn and Mn–Ni atoms. Low-temperature-grown thick Mn films exhibit a Stranski–Krastanov growth mode with a stable $(\sqrt{3} \times \sqrt{3})R 30^\circ$ reconstruction, which remains stable up to room temperature.

1. Introduction

Ultrathin magnetic films, because of the reduced dimensionality, exhibit distinguished magnetic properties with respect to the bulk.^[1–8] The morphology of such thin films can influence the magnetic properties significantly.^[9–11] The 3d transition metal Mn has drawn much attention in ultrathin magnetic film research in the last decades, not only because of its large atomic magnetic moment resulting from the half-filled *d* orbital, but also due to the diversity of phases when epitaxially grown on different substrates.^[12–22] The crystalline structure, in some way, determines the properties of thin films. When the impinging atoms reach a metal surface, the way they arrange to form a new structure on the substrate is often an interesting topic to

investigate. Depending on factors like, for example, temperature, thickness, substrate material, and symmetry, Mn could intermix with the substrate atoms and form ordered or disordered alloys.^[23–26] In some cases, alloys are only limited to the surface, such as Mn on Cu(100),^[27] Cu(110),^[28] Co(001),^[29] Ni(100),^[23,30] and Ni(110),^[13,26] while some alloys involve a few atomic layers, as in Mn/Ag(001).^[31] In other cases, like Mn on Fe(100)^[32,33] and Fe(110),^[34] no alloy is formed and only a pure Mn adlayer is found. Mn on Ni(111)/W(110) tends to have a disordered structure after 0.5 ML Mn deposition at room temperature, no intermixing between Mn and Ni has been observed.^[35] Annealing could introduce different ordered alloys of Mn and Ni in different Ni layers. For Mn on bulk Ni(111), there is still a lack of direct experimental evidence for how the Mn atoms arrange on this sixfold hexagonal substrate surface.


In this paper, we employ surface-sensitive techniques, namely scanning tunneling microscopy (STM), medium-energy electron diffraction (MEED), and low-energy electron diffraction (LEED) to systematically study ultrathin Mn films on Ni(111). Depending on the film thickness, the crystallographic structures of the Mn films vary significantly from submonolayer (ML) to a few MLs and transitions in the growth mode occur during the growth. Atomic-resolution STM imaging reveals the initial growth of Mn on Ni(111) and, together with LEED pattern analysis, suggests a size-dependent metastable lattice distortion of Mn islands with respect to the substrate. Moreover, the influence of temperature on the ML and thicker Mn films is also investigated.

2. Experimental Section

The experiments were carried out in an ultrahigh vacuum system with a base pressure of 1×10^{-10} mbar. The Ni(111) substrate was a disk-shaped single crystal with a diameter of 10 mm. To achieve a well-defined surface, the Ni(111) substrate was cleaned by cycles of Ar⁺ sputtering with ion energy of 1 keV at 700–750 K, followed by subsequent annealing at 950 K for 20–30 min. The cleanliness and smoothness of the crystal surface were examined by Auger electron spectroscopy, LEED, and STM. For the Mn thin-film deposition, molecular beam epitaxy was used. Mn was evaporated by electron bombardment of Mn pieces with 99.95% purity in a molybdenum crucible. An

Dr. J. Song, Prof. W. Kuch
Freie Universität Berlin
Institut für Experimentalphysik
Arnimallee 14, 14195 Berlin, Germany
E-mail: kuch@physik.fu-berlin.de

Dr. J. Song
School of Physics
Northwest University
Xuefu Avenue 1, 710127 Xi'an, China

 The ORCID identification number(s) for the author(s) of this article can be found under <https://doi.org/10.1002/pssb.201800173>.

DOI: 10.1002/pssb.201800173

in situ MEED setup (primary beam energy 3.0 keV, grazing incidence angle less than 5°) was used to monitor the film thickness change during the film growth. A room-temperature STM with a ring-shaped iron probe^[21,36] was employed for the STM characterization. All the STM images were obtained in the constant-current mode.

3. Results and Discussion

3.1. Growth of Mn on Ni(111) at Room Temperature

The topography of room-temperature-deposited Mn on Ni(111) depends on the thickness. In the sub-ML range, Mn atoms first form tiny scattered islands (4 ± 2 nm wide), the gaps between

which are gradually filled at higher coverages to form a wetting layer, as seen in **Figure 1a–c**. At the thickness of 1.7 ML, second-ML islands in **Figure 1d** become larger (7 ± 2 nm wide) and gaps are more uniformly distributed than those in the sub-ML range. Even larger patches (10–20 nm wide) are formed at 2.5 ML thickness in **Figure 1e**. Patches of similar size can be seen at 5.3 ML in **Figure 1f**. At the thickness of 8 and 12 ML, the surface morphology demonstrates a layer-plus-island growth mode and island growth mode, as shown in **Figure 1g** and **h**, respectively. **Figure 1i** shows the in situ MEED intensity curve recorded while depositing a thick Mn layer on Ni(111). The intensity drops during the first 75 s of Mn deposition, and then levels off at about 10–15% of the initial intensity. Three wiggles are discernible that can be assigned to the completion of the 1st, 3rd, and 4th ML, while a maximum related to the 2nd monolayer is hardly seen.

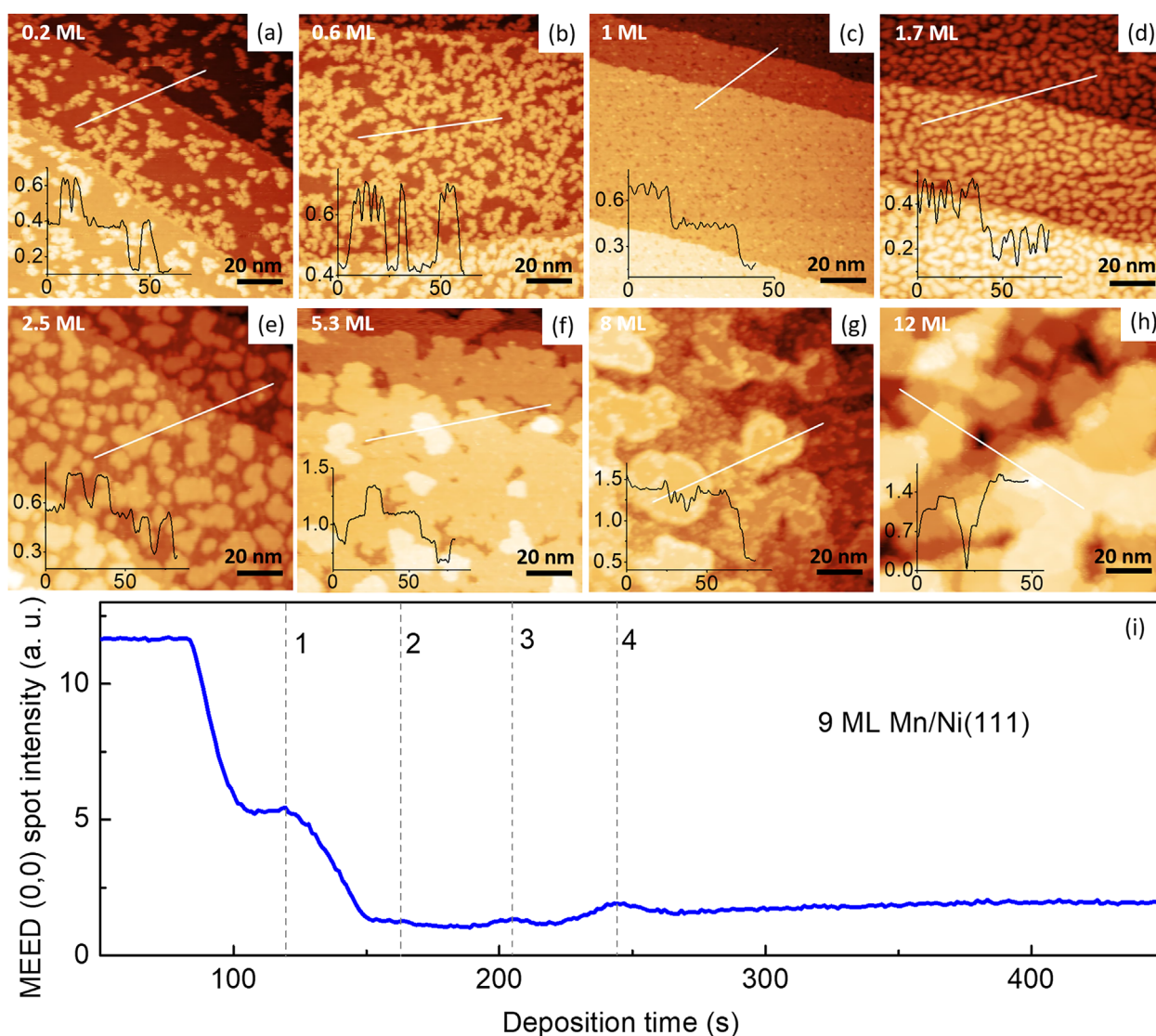


Figure 1. a–h) Constant-current STM topography images of room-temperature-deposited Mn on Ni(111) with thicknesses of 0.2, 0.6, 1, 1.7, 2.5, 5.3, 8, and 12 ML. i) MEED curve of the (0,0) spot intensity during the deposition of 9 ML Mn on Ni(111). Tunneling parameters: (a–h) +0.2 V, 1.9 nA; +0.2 V, 2.2 nA; +0.5 V, 1.1 nA; +0.2 V, 2.1 nA; +0.5 V, 1.4 nA; −0.2 V, 2.1 nA; +1.37 V, 0.49 nA; +0.5 V, 21 nA. The insets in (a–h) correspond to line profiles along the white lines in each image. Axis unit of insets: nm.

To obtain a deeper understanding of the sub-ML Mn lattice structure, **Figure 2a,b** present atomic-resolution imaging of the as-grown 0.2 ML Mn/Ni(111) surface. The two images were taken from the same sample but different areas. The time interval between measuring the two images is short to ensure similar conditions of the STM piezo scanner. To do the 2D fast Fourier transforms (FFT), we selected two areas in the Ni and Mn regions separately. The 2D FFT of the Ni and Mn areas shown in the insets of **Figure 2a,b** reveal that the lattice of sub-ML Mn islands does not conserve the substrate lateral lattice constant, but assumes a $(31 \pm 10)\%$ larger lattice constant. This is confirmed by LEED images for the clean Ni(111) substrate (**Figure 2c**) and for Mn coverages of 0.6 and 1.0 ML (**Figure 2d** and **e**, respectively). Above 1 ML, no LEED diffraction patterns are observed at room temperature. The LEED pattern for 1 ML Mn exhibits less diffuse background and the distance between opposite diffraction spots in **Figure 2e** appears slightly smaller compared to the substrate. This can be seen from **Figure 2f**, which presents line profiles through the LEED images taken along the white lines in **Figure 2c–e**. The line profiles have been aligned at the left spot. The distance between opposite diffraction spots is reduced by $(4.3 \pm 0.25)\%$ at 1 ML Mn coverage compared to Ni(111). Moreover, the Mn lattice is not a regular hexagonal one, but laterally distorted, as becomes most obvious when looking at the inset of **Figure 2b**.

We observe thus a layer-by-layer growth mode in the initial stages of Mn deposition, up to about 5 ML, which then, possibly

gradually, is reduced at higher thicknesses until at 12 ML up to eight layers are simultaneously exposed. Despite the initial layer-by-layer growth, even the first ML of Mn does not assume the lateral lattice periodicity of the Ni(111) substrate, but exhibits an incommensurate, laterally distorted hexagonal structure with larger lattice constant. This has to be attributed to the large lattice mismatch to the fcc Ni(111) surface.

Despite the layer-by-layer growth seen from the STM images, the reflected electron intensity during deposition does not show pronounced oscillations. The intensity after completion of the first ML is distinctly higher than during deposition of the following layers, which could be related to a structural transition after the completion of the first layer. This would also explain why the peak corresponding to the completion of the second ML is hardly visible, while the ones for the third and fourth ML are more clearly distinguished.

Taking into account the STM data, we attribute the background intensity in the LEED image of 0.6 ML Mn to the structural distortion of the Mn crystallographic structure within the islands on Ni(111). The degree and orientation of the distortion may vary from island to island. While the Mn wetting layer at 1 ML coverage tends to have a certain orientation of lattice distortion with respect to the Ni(111) substrate, this is different in the randomly oriented Mn islands when the coverage is below 1 ML. A disordered interfacial alloying could in principle also be the cause of the LEED background intensity, although no intermixing between Mn and Ni was found after room-temperature deposition of Mn on 4 ML Ni/W(110).^[35]

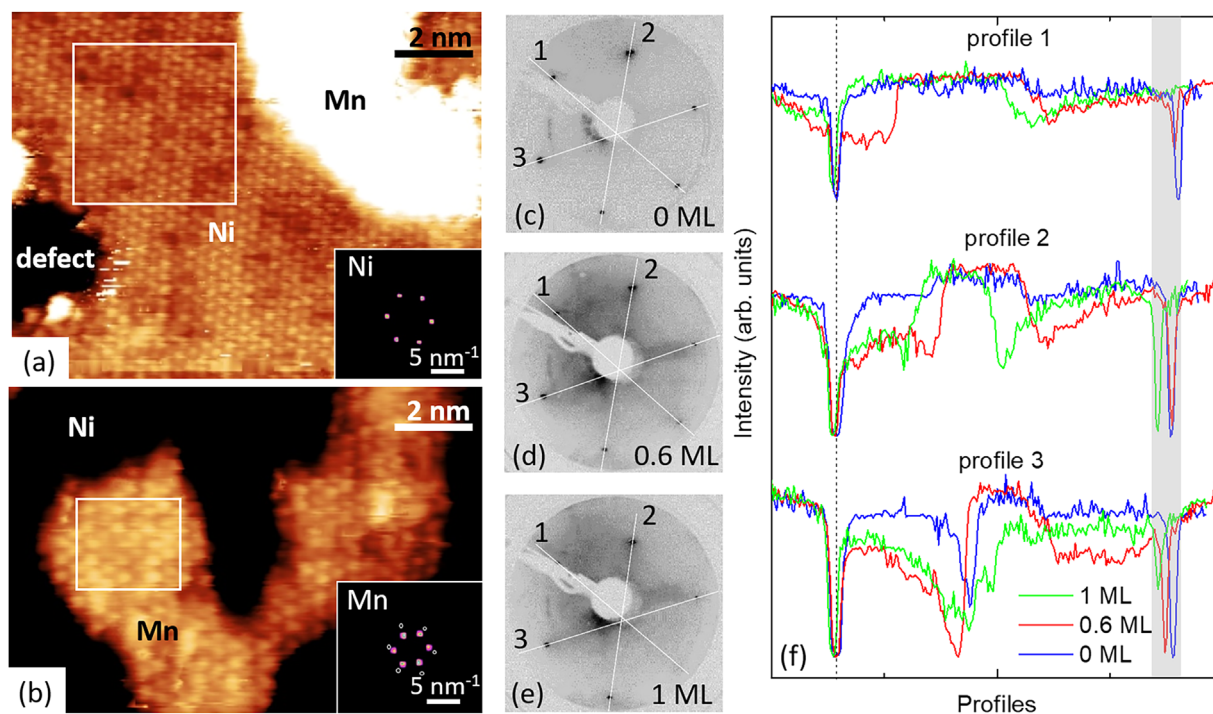


Figure 2. Atomic-resolution constant-current STM images for 0.2 ML Mn/Ni(111) showing the Ni substrate (a) (+25 mV, 2.2 nA) and a Mn island (b) (+49 mV, 2.8 nA) with enhanced contrast. Insets show the 2D FFT of the corresponding STM images for Ni(111) and Mn/Ni(111) in the regions marked by white rectangles. The white circles in the inset of (b) represent the superimposed 2D FFT pattern of the inset of (a). c–e) LEED patterns taken at 120 eV for Ni(111), room-temperature-deposited 0.6 ML Mn/Ni(111), and 1 ML Mn/Ni(111). f) Line profiles taken from (c–e), as marked by the numbered white lines in each image, respectively.

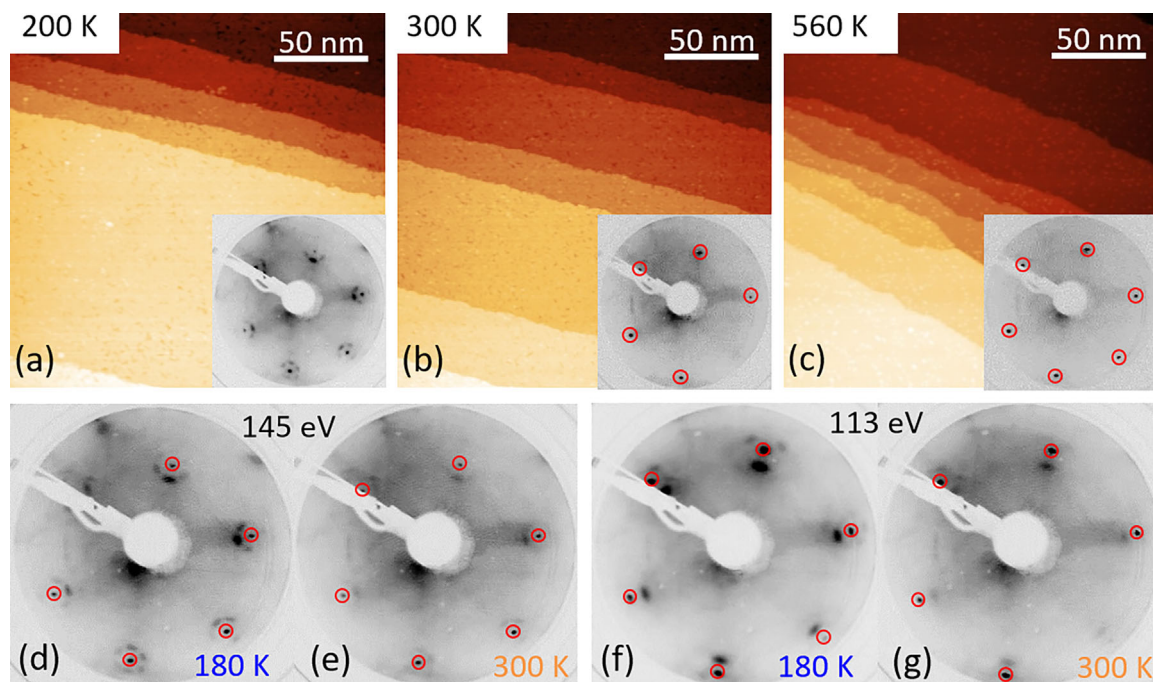


Figure 3. a–c) Room-temperature constant-current STM images of 1 ML Mn/Ni(111) prepared at 200, 300, and 560 K, respectively. Tunneling parameters: +1.1 V, 0.49 nA. The inset of (a) shows the LEED pattern taken at 180 K, 150 eV. Insets of (b) and (c) are corresponding LEED patterns both taken at room temperature, 120 eV. d, f) LEED patterns at 145 and 113 eV, respectively, for sample in (a) taken at 180 K. e, g) LEED patterns at 145 and 113 eV, respectively, after the sample in (a) was annealed from 180 to 300 K. Red circles in the LEED patterns mark the hexagonal $p(1 \times 1)$ diffraction spots.

3.2. The Influence of Temperature on the Growth of a Monolayer Mn on Ni(111)

Temperature plays an important role for thin-film deposition.^[37–41] Since 1 ML is a critical thickness for room-temperature-deposited Mn/Ni(111), the change of the crystallographic structure of Mn with 1 ML thickness at different temperatures is an interesting topic to be discussed. **Figure 3** shows the result of the characterization by room-temperature STM and LEED of 1 ML Mn on Ni(111), deposited at

different temperatures. STM topography images for deposition at 200, 300, and 560 K show complete, smooth Mn wetting layers on the nickel substrate. LEED patterns of Mn deposited at different temperatures, in contrast, exhibit diverse features. For growth at 200 K, the pattern displays sixfold superstructure satellite spots around each of the substrate diffraction spots marked by red circles. At both, 300 and 560 K growth temperatures, only sharp diffraction spots from the substrate are present. The difference between the 560- and 300-K LEED patterns is the much lower background of the

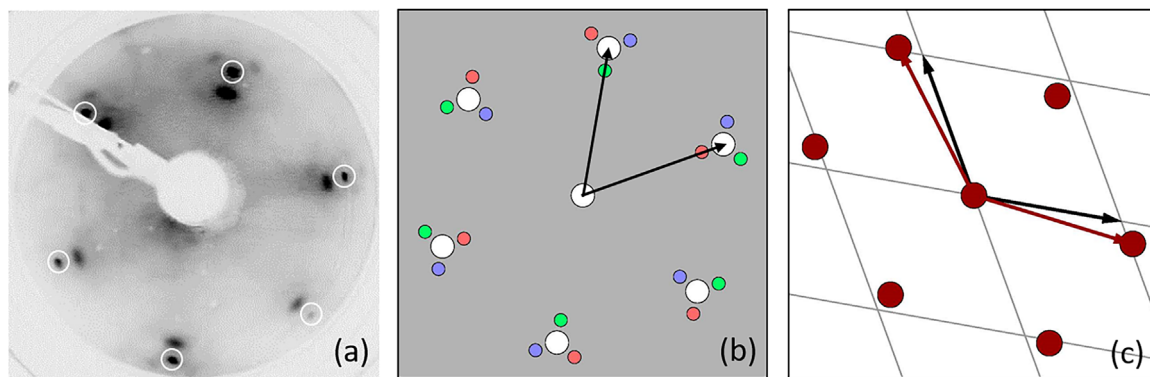


Figure 4. a) LEED pattern from **Figure 3f**. b) Simulated LEED pattern of (a). Three different domains are marked by pink, green, and blue colors. White spots show the hexagonal $p(1 \times 1)$ diffraction spots, black arrows represent vectors of the reciprocal unit cell of the substrate. c) Simulated real-space lattice for (b). Only one domain, corresponding to the blue spots in (b), is shown. The gray grid represents the Ni(111) substrate lattice, red dots indicate Mn atoms. Black arrows show the substrate unit cell vectors, red arrows the film unit cell vectors.

former, indicating a well-ordered (1×1) hexagonal lattice for high-temperature-deposited Mn. After annealing the 200-K-prepared Mn layer from 180 to 300 K, the superstructure in the LEED image is strongly diminished and only the inner dim satellite spots remain, as shown in Figure 3d,e and f,g at 145 and 113 eV, respectively. Note that the LEED superstructure observed on the 200-K-prepared Mn/Ni(111) around the substrate lattice diffraction spots exhibits six- and threefold symmetries at 145 and 113 eV, respectively, with satellite spot separation 0.13 ± 0.01 of that of the substrate spots, and will be discussed below. We exclude residual gas as the cause for the superstructure because the chamber pressure was always kept below 3×10^{-10} mbar to avoid such contamination. Similar sixfold superstructures on the (111) surface have also been observed in other systems, such as Ag/Ni(111)^[38,42,43] and Ag/Cu(111).^[44] The scenario for superstructure formation in these systems is a rotated Ag lattice with respect to the substrate in a high-temperature-deposited Ag layer (> 300 K). Interestingly, in Mn/Ni(111), the six- and threefold satellite superstructures are observed only for low-temperature growth and disappear after annealing to higher temperatures, in contrast to the sixfold satellite superstructures reported for Ag/Ni(111) by Chambon et al.,^[38] where the room-temperature- or 400-K-deposited Ag films are poorly ordered and the sixfold superstructure appears only after annealing to higher temperatures.

To explain the LEED superstructure observed on low-temperature-grown ML-thick Mn/Ni(111), we suggest an incommensurate lattice resulting from a uniaxial distortion similar to that of the room-temperature-deposited sub-ML Mn/Ni(111) seen in the inset of Figure 2b: The ratio between the real-space overlayer lattice vector and the basic lattice vector is 1.113 and the two overlayer lattice vectors are rotated 7° counterclockwise and clockwise, respectively, as the red arrows illustrate in Figure 4c. A simulation of the LEED pattern resulting from that two-dimensional structure using the LEEDpat^[45] software is shown in Figure 4b, along with the experimental LEED image (Figure 4a). Differently from STM, LEED reflects the lattice structure in a much larger area. Differently oriented structural domains have thus to be considered. For the simulated pattern of Figure 4b, three individually oriented domains with a mutual angle of 120° have been used and the resulting spots marked by separate colors. The domain of the Mn lattice drawn in real space (Figure 4c) corresponds to the blue diffraction spots in Figure 4b.

While the 200-K-grown Mn layer exhibits a superstructure in the LEED pattern also at 1 ML coverage, the room-temperature-grown layers at 0.6 and 1 ML Mn thickness do not, as seen from Figure 2d,e, while the 2D FFT pattern from Mn islands at 0.2 ML does, see the inset of Figure 2b. Different structures at higher submonolayer coverages at different growth temperatures could result from different adsorption sites of the Mn atoms with respect to the Ni substrate atoms, metastable in the case of growth at 200 K, leading to different Mn–Mn and Mn–Ni distances and thus to a different arrangement of the Mn adlayer, similar as discussed for alkali-adlayer/metal systems.^[46] The change in the LEED satellite superstructure in the 200-K-deposited Mn/Ni(111) system between sixfold (Figure 3d) and threefold (Figure 3f) may be explained by interference with electrons scattered from the fcc substrate lattice below the Mn layer, which is not considered in the simple simulation shown in

Figure 4b, resulting in the disappearance of three of the satellite spots. The slightly stronger diffuse background of the LEED pattern of the 300-K-grown Mn ML (inset of Figure 3b) compared to that of the 560-K-grown layer (inset of Figure 3c) indicates

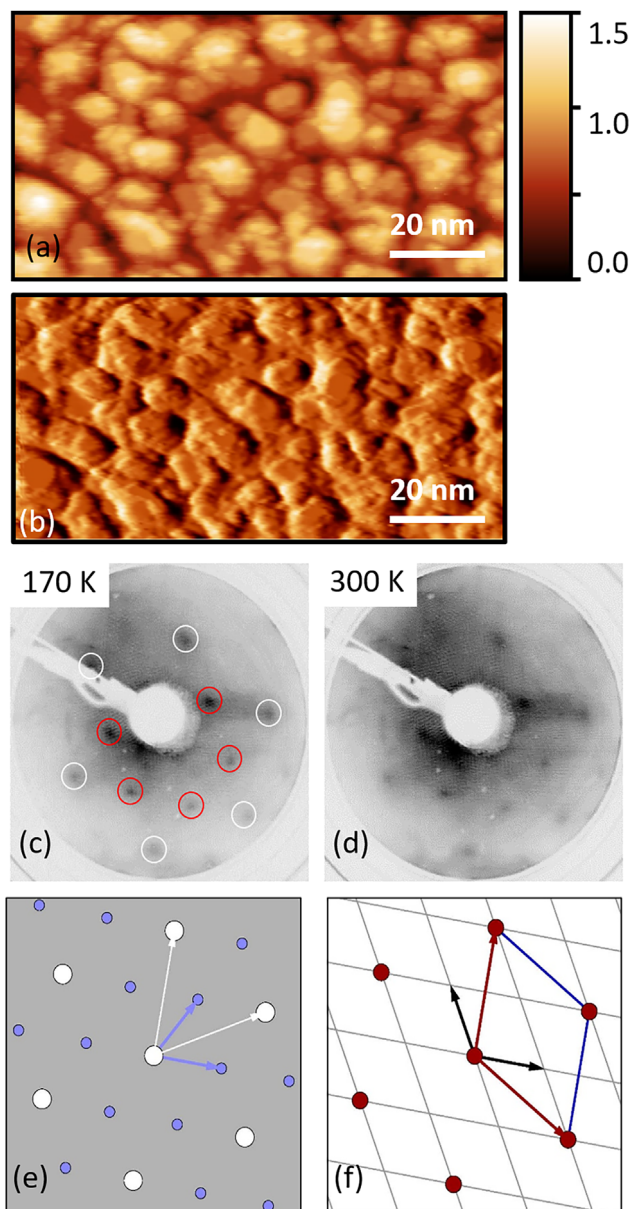


Figure 5. a) Room-temperature STM topography image for 170-K-deposited 8 ML Mn on Ni(111). Tunneling parameters: +0.2 V, 2.16 nA. The color bar unit: nm. b) Differentiated image of (a). c, d) LEED patterns for (a) taken at 170 K and after annealing to room temperature, respectively. Electron energy for both patterns is 120 eV. White circles show the positions of hexagonal $p(1 \times 1)$ spots and red circles mark the diffraction spots of the superstructure. e) Simulated LEED pattern of (c). White and blue arrows represent reciprocal unit cell vectors for substrate and overlayer, respectively. f) Simulated real-space lattice for (e). The red dots and crossing points of the gray grid are for topmost and top second Mn atoms, respectively. Black arrows show the grid-layer unit-cell vectors, red arrows the dot-layer superlattice unit-cell vectors.

some structural disorder in the former, possibly resulting from a transition between the structurally distorted layer found at lower growth temperatures and the isostructural layer found at higher growth temperature. No superstructure is seen in the LEED pattern of the 560-K-grown layer (inset of Figure 3c), which has a very low background. This means that at such high temperature, the film assumes the structure of the substrate. As seen from the LEED images of Figure 3, heating 1 ML Mn deposited at 200–300 K does not result in the same structure as depositing 1 ML at 300 K. In the latter case some satellite spots are still visible. This could be explained by the hindrance of neighboring Mn atoms in a full ML to reach the energetically more favorable isostructural case, as during deposition at higher temperatures.

3.3. Low-Temperature-Grown Thick Mn Film on Ni(111)

As discussed before, a ML Mn exhibits a metastable laterally distorted lattice when deposited at 200 K. How does the crystallographic structure arrange in thick Mn films deposited at low temperature? Figure 5a shows an STM topography image of 8 ML Mn deposited at 170 K on Ni(111). The surface, with a roughness of about 1.5 nm, exhibits a Stranski–Krastanov (SK) growth mode. The island edges can be more clearly seen in the differentiated image in Figure 5b. For low-temperature deposition, one main difference between 1 ML and a thick film of Mn is the stable ordered phase of the latter. According to the LEED pattern shown in Figure 5c, 8 ML Mn on Ni(111) exhibits diffuse (1×1) hexagonal diffraction spots with some superstructure. This superstructure is identified as a $(\sqrt{3} \times \sqrt{3})R 30^\circ$ reconstruction, as illustrated by the simulated LEED pattern in Figure 5e. The reconstruction, schematically shown in real space in Figure 5f, remains present after annealing the film to 300 K, except for a stronger diffuse background. We take this as an evidence for a stable lattice structure in the thick Mn film. The simulation of the LEED image does not require any incommensurate lattice distortion in the overlayer, and the phase for a thick Mn layer differs from that of thin layers discussed before.

4. Conclusion

In conclusion, we have investigated the growth of Mn on Ni(111) from the aspects of thickness and temperature. Mn deposition at room temperature on Ni(111) exhibits a layer-by-layer growth up to 5.3 ML. In the layer-by-layer-growth thickness range, the size of Mn islands depends on thickness. Atomic-resolution imaging of sub-ML Mn/Ni(111) reveals a laterally distorted Mn lattice, while the LEED study suggests a relatively smaller distortion in the Mn wetting layer than in 0.2 ML Mn islands. At the thickness of 1 ML, the low-temperature-deposited Mn film shows a metastable lattice distortion. This metastable phase becomes less distorted when the temperature is increased to 300 K. The reason could be a temperature-dependent metastable arrangement of the Mn adlayer as well as the different interaction strength between Mn–Mn and Mn–Ni atoms. According to a stronger diffuse background of the LEED pattern, the 300-K-deposited ML Mn demonstrates some structural disorder at room temperature. On the contrary, the (1×1) LEED pattern of the 560-K-grown ML Mn indicates weak or no lateral lattice

distortion. As to thick Mn films on Ni(111), we have observed an SK growth mode at low temperature. The as-grown film exhibits a $(\sqrt{3} \times \sqrt{3})R 30^\circ$ reconstruction which remains stable from low to room temperature. The simulated real-space lattice shows no incommensurate lattice distortion in the overlayer, which demonstrates a stable lattice structure for thick Mn films.

Acknowledgement

J.S. acknowledges financial support by the China Scholarship Council (Grant No. 2011628009).

Conflict of Interest

The authors declare no conflict of interest.

Keywords

manganese, structural transitions, superstructures, thin films

Received: April 17, 2018

Revised: July 1, 2018

Published online:

- [1] M. Bode, M. Heide, K. von Bergmann, P. Ferriani, S. Heinze, G. Bihlmayer, A. Kubetzka, O. Pietzsch, S. Blügel, R. Wiesendanger, *Nature* **2007**, 447, 190.
- [2] J. S. Park, A. Quesada, Y. Meng, J. Li, E. Jin, H. Son, A. Tan, J. Wu, C. Hwang, H. W. Zhao, A. K. Schmid, Z. Q. Qiu, *Phys. Rev. B* **2011**, 83, 113405.
- [3] U. Bauer, M. Dąbrowski, M. Przybylski, J. Kirschner, *Phys. Rev. B* **2011**, 84, 144433.
- [4] Y. Yoshida, S. Schröder, P. Ferriani, D. Serrate, A. Kubetzka, K. von Bergmann, S. Heinze, R. Wiesendanger, *Phys. Rev. Lett.* **2012**, 108, 087205.
- [5] A. Brataas, A. D. Kent, H. Ohno, *Nat. Mater.* **2012**, 11, 372.
- [6] S. Parkin, S.-H. Yang, *Nat. Nanotechnol.* **2015**, 10, 195.
- [7] D. Weber, L. M. Schoop, V. Duppe, J. M. Lippmann, J. Nuss, B. V. Lotsch, *Nano Lett.* **2016**, 16, 3578.
- [8] J.-Y. Chen, J. Zhu, D. Zhang, D. M. Lattery, M. Li, J.-P. Wang, X. Wang, *J. Phys. Chem. Lett.* **2016**, 7, 2328.
- [9] W. Kuch, L. I. Chelaru, F. Offi, J. Wang, M. Kotsugi, J. Kirschner, *Nat. Mater.* **2006**, 5, 128.
- [10] T. Allmers, M. Donath, *New J. Phys.* **2009**, 11, 103049.
- [11] S.-H. Phark, J. A. Fischer, M. Corbetta, D. Sander, K. Nakamura, J. Kirschner, *Nat. Commun.* **2014**, 5, 5183.
- [12] M. Wuttig, Y. Gauthier, S. Blügel, *Phys. Rev. Lett.* **1993**, 70, 3619.
- [13] O. Rader, T. Mizokawa, A. Fujimori, A. Kimura, *Phys. Rev. B* **2001**, 64, 165414.
- [14] M. Bode, S. Heinze, A. Kubetzka, O. Pietzsch, M. Hennefarth, M. Getzlaff, R. Wiesendanger, X. Nie, G. Bihlmayer, S. Blügel, *Phys. Rev. B* **2002**, 66, 014425.
- [15] S. Gallego, F. Soria, M. C. Muñoz, *Surf. Sci.* **2003**, 524, 164.
- [16] M. Scarselli, L. Dragone, A. Sgarlata, M. Fanfoni, V. Di Castro, R. Zanon, *Surf. Sci.* **2003**, 545, L774.
- [17] B. R. Malonda-Boungou, B. M'Passi-Mabiala, A. Debernardi, S. Meza-Aguilar, C. Demangeat, *Phys. Rev. B* **2010**, 81, 024402.
- [18] S. Sachert, S. Polzin, K. Kostov, W. Widdra, *Phys. Rev. B* **2010**, 81, 195424.

- [19] P. Mishra, T. Uchihashi, T. Nakayama, *Appl. Phys. Lett.* **2011**, 98, 123106.
- [20] T. Suzuki, T. Lutz, B. Geisler, P. Kratzer, K. Kern, G. Costantini, *Surf. Sci.* **2013**, 617, 106.
- [21] J. Song, C.-B. Wu, B. Zhang, J. Xu, W. Kuch, *Phys. Rev. B* **2015**, 91, 214406.
- [22] P. Matvija, P. Sobotík, I. Ošťádal, P. Kocán, *Appl. Surf. Sci.* **2015**, 331, 339.
- [23] M. Wuttig, C. C. Knight, T. Flores, Y. Gauthier, *Surf. Sci.* **1993**, 292, 189.
- [24] B.-C. Choi, P. J. Bode, J. A. C. Bland, *Phys. Rev. B* **1998**, 58, 5166.
- [25] J. Schneider, A. Rosenhahn, K. Wandelt, *Appl. Surf. Sci.* **1999**, 142, 68.
- [26] L. Deng-Feng, X. Hai-Yan, Z. Xiao-Tao, D. Hui-Ning, G. Fei, *Chin. Phys. B* **2010**, 19, 087102.
- [27] R. G. P. van der Kraan, H. van Kempen, *Surf. Sci.* **1995**, 338, 19.
- [28] U. Manju, D. Topwal, G. Rossi, I. Vobornik, *Phys. Rev. B* **2010**, 82, 035442.
- [29] P.-J. Hsu, C.-I. Lu, Y.-H. Chu, B.-Y. Wang, C.-B. Wu, L.-J. Chen, S.-S. Wong, M.-T. Lin, *Phys. Rev. B* **2012**, 85, 174434.
- [30] M. Wuttig, T. Flores, C. C. Knight, *Phys. Rev. B* **1993**, 48, 12082.
- [31] P. Schieffer, M. C. Hanf, C. Krembel, G. Gewinner, *Surf. Sci.* **2000**, 446, 175.
- [32] T. G. Walker, H. Hopster, *Phys. Rev. B* **1993**, 48, 3563.
- [33] D. Spišák, J. Hafner, *Surf. Sci.* **2007**, 601, 4348.
- [34] O. Rader, C. Pampuch, W. Gudat, A. Dallmeyer, C. Carbone, W. Eberhardt, *Europhys. Lett.* **1999**, 46, 231.
- [35] M. A. J. Allen, D. Venus, *Surf. Sci.* **2001**, 477, 209.
- [36] C.-B. Wu, J. Song, W. Kuch, *Appl. Phys. Lett.* **2012**, 101, 012404.
- [37] R. T. Vang, K. Honkala, S. Dahl, E. K. Vestergaard, J. Schnadt, E. Lægsgaard, B. S. Clausen, J. K. Nørskov, F. Besenbacher, *Surf. Sci.* **2006**, 600, 66.
- [38] C. Chambon, J. Creuze, A. Coati, M. Sauvage-Simkin, Y. Garreau, *Phys. Rev. B* **2009**, 79, 125412.
- [39] V. S. Zhigalov, V. G. Myagkov, O. A. Bayukov, L. E. Bykova, G. N. Bondarenko, A. A. Matsynin, *JETP Lett.* **2009**, 89, 621.
- [40] S. Mathuri, K. Ramamurthi, R. Ramesh Babu, *Thin Solid Films* **2017**, 625, 138.
- [41] K. Dragounová, T. Ižák, A. Kromka, Z. Potůček, Z. Bryknar, Š. Potocký, *Appl. Phys. A* **2018**, 124, 219.
- [42] L. G. Feinstein, E. Blanc, D. Dufayard, *Surf. Sci.* **1970**, 19, 269.
- [43] S. Mróz, Z. Jankowski, M. Nowicki, *Surf. Sci.* **2000**, 454, 702.
- [44] E. Bauer, *Surf. Sci.* **1967**, 7, 351.
- [45] K. Hermann, M. A. Van Hove, LEEDpat4 (LEED pattern analyzer) **2016**.
- [46] J. N. Andersen, E. Lundgren, R. Nyholm, M. Qvarford, *Surf. Sci.* **1993**, 289, 307.